Energy Conversion and Management 344 (2025) 120204

Contents lists available at ScienceDirect

Energy Conversion and Management

journal homepage: www.elsevier.com/locate/enconman

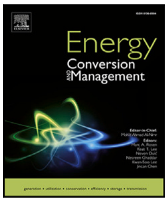

Minimizing Levelized Cost of Energy and visual impact in Mediterranean offshore wind farms: A multi-objective optimization approach

V.F. Barnabei *, M. Conti, T.C.M. Ancora, G. Delibra, A. Castorrini, F. Rispoli, A. Corsini

Department of Mechanical and Aerospace Engineering, Sapienza University of Rome, Rome, Italy

ARTICLE INFO

Keywords:
Wind farm
Layout optimization
NSGA II
AEP
Visual impact
LCOE
Wind energy

ABSTRACT

Offshore wind farms are emerging as a key power plant option for EU's transition to net-zero emissions by 2050. With the growing trend of installing large turbines in multi-gigawatt farms, increasing attention is being given to the visual impact perceived from the coast. This study introduces an optimization method that incorporates visual impact as a social-acceptance indicator and the Levelized Cost of Energy to provide a comprehensive techno-economic sustainability assessment for offshore wind projects. The method resolves a multi-objective and multi-constrained wind farm layout optimization problem in a designated marine area. The number of turbines is one of the independent variables in each studied wind farm and multiple points of observation from the shoreline are contributing to the evaluation on visual impact. The case study is represented by a virtual wind farm located in the Mediterranean Sea, with 15 MW turbines. The results yield a Pareto front, with the trade-off solution represented by a farm with 13 turbines, distributed regularly, and a Levelized Cost of Energy of 110.73 €/MWh. Additionally, four comparative analyses are performed to evaluate the effect of (i) different turbine sizes, (ii) different wake loss models, (iii) different wind data source and (iv) different wind farm areas.

1. Introduction

To achieve the target of net zero emissions [1], underlined by the REpowerEU plan [2], the European Commission foresees an installation capacity of 300 GW for offshore wind by 2050 [3]. Interest in the development of offshore wind technologies is driven by the availability and quality of the wind energy source. Additionally, economic sustainability of this technology is expected to grow by using fewer but larger wind turbines (WTs), which reduces costs associated with installation, substructures and maintenance. Larger turbines also minimize the number of required components, such as foundations, cables, and offshore substations, while simplifying project design. As a result, 15 MW turbines are becoming the industry standard and some manufacturers are exploring up to 22 MW [4].

However, offshore installations face multiple constraints as many coastal regions are nature protection areas, due to wildlife and landscapes, or areas with intense anthropic activities, either economic or social. Restrictions on areas used for human activities, such as fishing and navigation, combined with a non-negligible Visual Impact (VI) experienced from the coast, spark considerable public opposition to offshore wind installations [5], and for this reason are being considered more frequently as a key parameter in the process of offshore wind projects allocation rounds [6]. Significant concerns about visual disamenities, which may also affect tourism, continue to be a focal point when presenting offshore wind farm projects to local coastal communities. In contrast, other potential impacts, such as operational noise emissions, are of minor importance for offshore installations compared to onshore ones [7]. Consequently, it is essential to consider those social aspects when designing an offshore wind farm. Specifically, the deployment of large turbines can result in a significant VI experienced from the coast. At the same time, the effort to minimize VI may result in highly compact turbine clusters and a consequent reduction in energy yield due to a strong rotor-wake interaction. From the mentioned considerations emerges the interest to evaluate alternative layouts beyond the conventional regular configurations commonly adopted in offshore installations. In regular layouts, as demonstrated by Hou et al. wind turbine wake interaction losses can lead to a reduction of Annual Energy Production (AEP) by approximately 15% compared to an ideal scenario without wake-rotor interactions [8]. More complex turbine distributions could enable greater exploitation of the wind resource without increasing the spatial footprint of wind farms.

Therefore, the aim of this work is to build an effective layout design method that balances both objectives by setting an adequate spacing

---

* Corresponding author.
E-mail address: valerio.barnabei@uniroma1.it (V.F. Barnabei).

https://doi.org/10.1016/j.enconman.2025.120204

of turbines to reduce VI while enabling them to operate in wake-free conditions for most of their operational time. When proposing alternative layouts, it is important to account for site-specific features, such as the bathymetric profile and the distance from the coast, which influence costs and impacts. At the same time, constraints such as the minimum and maximum number of turbines, as well as the minimum distance between them, must be respected. This allows the determination of an optimal layout within the available marine space perimeter, balancing various project objectives and spatial constraints, defining a multi-constrained and multi-objective optimization problem.

Wind farm layout optimization is a widely covered topic by the open literature to date. The various approaches differ in the objective functions chosen and in the selected optimization algorithms [9]. Many studies focus on maximizing the energy or power output of the wind farm [10], while others introduce methods to calculate installation and maintenance costs of the latter, to evaluate economic indicators, e.g. Net Present Value (NPV) [11] or the Levelized Cost of Energy (LCOE) [12]. Additionally, there are various examples of multi-objective optimizations: Chen et al. [13], consider as objectives the cost per power unit and efficiency; Guirguis et al. [14] maximize the AEP while minimizing land use and transmission cable length; Li et al. [15] use the AEP, the Euclidean distance between turbines, and the layout perimeter as objective functions; Biswas et al. [16] consider the efficiency and power output of the wind farm; Moreno et al. [17] include the occupied area, the LCOE, and the efficiency; Barnabei et al. [18] consider the AEP and the total costs. Dinçer et al. [19] integrate Analytical Hierarchy Process (AHP) and Geographic Information System (GIS) tools into a multi-objective optimization that considers energy production, costs, and environmental factors such as bird migration paths; Kim et al. [20] use a genetic algorithm to maximize energy production while minimizing hourly fluctuations caused by wind intermittency; Zhang et al. [21] optimize wind farm layout to maximize efficiency while minimizing turbine loads, estimated through a surrogate model. Moreover, many different kind of algorithms are proposed from literature: combinations of Mixed Integer Linear Programming (MILP) models and heuristic methods [22], Self-organizing Map (SOM) based methods [23], topology based algorithms [24], Particle Swarm Optimization (PSO) [25], and Genetic Algorithms (GA) [18].

While these studies have provided valuable insights, certain aspects still require further exploration. Wind farm layout optimization often focuses solely on turbine placement while keeping the total farm size fixed. In contrast, in this study the wind farm size is an optimization output, and it is obtained allowing the number of turbines to vary freely within a defined range. Therefore, this study presents a method to solve a multi-objective and multi-constrained layout optimization problem, aiming to maximize economic return, reducing LCOE, and minimize VI experienced by coastal communities without fixing the nominal power of the wind farm. The selection of LCOE and VI as the objective functions for the optimization algorithm is driven by the inherently adversarial nature of these targets. Minimizing LCOE typically involves increasing the number of turbines, as this increases AEP more than the associated costs. However, the same action simultaneously maximizes VI, saturating the field of view. On the other hand, a reduction in VI can be achieved by decreasing the number of turbines and arranging them in rows. However, this leads to increased wake losses and reduced AEP, which in turn drives up LCOE. For this purpose, the method relies on the non-deterministic genetic algorithm NSGA II [26], implemented in the open-source Python library PyMoo [27]. NSGA II generates a population of individuals (representing possible wind farm layouts) and allows them to evolve over generations, minimizing the values of the two objective functions of the problem (i.e., VI and LCOE). For a fixed external perimeter of the selected marine space, each layout represents a potential wind farm configuration characterized by a different number of turbines and their positions. Problem constraints are set on the minimum and maximum number of turbines, and the minimum distance between them. For each feasible layout, the LCOE is obtained by calculating the energy production over the life cycle of the facility and the discounted costs of CAPital EXpenditures (CAPEX) and OPerational EXpenditures (OPEX).

A strict requirement in layout optimization problems is the need to model the effects of wake-induced velocity reduction in order to evaluate the AEP of different configurations. This requirement can be met by adopting two alternative methods: Computational Fluid Dynamics (CFD) based tools and reduced-order analytical models. The former guarantees a high level of accuracy at the expense of highly demanding computational efforts. Hence, it is inferred that they are not well-suited for layout optimization purposes, which requires a high amount of different time-efficient evaluations of produced energy in extensive wind farms across numerous iterations. Reduced-order wake models, on the other hand, can easily tackle this computational challenge. Their definition and validation remain an open issue: since the introduction of the first linear wake expansion model proposed by Jensen in 1983 [28] to date, many models have been proposed. In particular, the most recent models advocate the modelling of velocity defect within the wake as a Gaussian distribution in the spanwise direction [29–31]. In the present work, the open-source tool “FLOw Redirection and Induction in Steady State” (FLORIS) [32] is used to estimate AEP. FLORIS includes different reduced-order wake models to evaluate wake losses under various wind conditions to which the farm is subjected. For the selected area, wind data is obtained from Global Wind Atlas (GWA) [33], as a wind frequency rose. Additionally, the AEP evaluation along the wind farm useful life incorporates a power derating model for erosion damage suffered by the turbine blades.

The cost model is based on models available in literature, merging the contributions by Martinez [34], Myhr [35], Cavazzi [36], Giglio [37], Allen [38] and Bjerk [39]. The model incorporates both site-specific factors and turbine positioning considerations, including the depth at each location to evaluate mooring costs. Other site-dependent factors are included, such as the distance to the shore to evaluate the export cable cost and the distance from the deployment port to estimate installation costs.

The visual impact is assessed with the model proposed by Gonzalez et al. [40], enhanced to evaluate VI from multiple observation points and considering the orientation of each turbine.

Weaknesses and measurement inaccuracies of the proposed method are certainly present, mainly due to the wake model’s low fidelity and the variability in wind source data. Nevertheless, these choices were necessary to handle the complexity of such a large-scale optimization problem, where the number of possible layouts makes computational efficiency a priority. The developed method is particularly relevant for early-stage industrial wind farm design and large-scale marine spatial planning, offering a practical tool for decision-making. Unlike traditional approaches based solely on technical-economic assessments through LCOE, it also incorporates social considerations, introducing a novel perspective in the industrial context. By providing a structured approach to optimizing offshore wind farm layouts, this study contributes to improving resource planning and informing energy policies, offering insights that align with industry needs and facilitate the large-scale deployment of offshore wind projects.

The present paper is organized as follows: Section 2 describes the methods used. Specifically, Section 2.1 presents the problem formulation and its implementation using NSGA II. Section 2.2 describes the visual impact model, Section 2.3 the wind farm performance model, and Section 2.4 the cost model (both for CAPEX and OPEX). Section 3 introduces the case study, with a description of the specific optimization parameters, wind conditions, bathymetric profile, and locations of observation points, offshore substation, and reference port. Section 4 illustrates the main quantitative findings and presents sensitivity and scalability analyses. Finally, Section 5 summarizes the conclusions of the paper.

2. Methods

The following section presents the optimization method, providing details of the implemented genetic algorithm and comprehensive definitions of the objective functions, describing VI, AEP and costs (thus LCOE) models.

2.1. Problem and algorithm description

The implemented optimization algorithm creates an initial random population of individuals, each representing a potential layout. The subsequent generations are then evolved by selecting individuals that demonstrate the best fit to the objective functions. In order to apply this method, the case study area is divided into a grid of nodes, each corresponding to a potential location for the turbines. The individual generated by the algorithm, given n the number of grid nodes, consists of a binary list $v = \{v_1, \dots, v_i, \dots, v_n\}$, where the elements are equal to 1 if the turbine is present, zero if not. Fig. 1 shows the representation of a layout together with its respective binary list. In the figure, black digits represent the index position i of each node in the list, while blue digits indicate the presence of the turbine. A bathymetric map of the selected area, obtained from Global Wind Atlas [33], is superimposed on this grid, with the aim of associating the depth of the water with each position. For each layout, the following objective functions are evaluated:

$$f_1 = \text{LCOE} \qquad f_2 = \text{VI} \tag{1}$$

where VI represents the visual impact indicator, defined in Section 2.2. LCOE is defined as the constant price per megawatt-hour (MWh) of energy required to recover the construction and operating costs of a generation plant over its lifecycle, and it is expressed as follows:

$$\text{LCOE} = \frac{\sum_{i=1}^{LT} (\text{CAPEX}_i + \text{OPEX}_i)(1+r)^{-i}}{\sum_{i=1}^{LT} \text{AEP}_i (1+r)^{-i}} \tag{2}$$

where LT is the life span of the wind farm and r is the discount rate. The following functions act as constraints of the optimization problem:

$$\begin{aligned} g_1 &: n_{\text{tur}} - N_{\text{max}} \le 0 \\ g_2 &: N_{\text{min}} - n_{\text{tur}} \le 0 \\ g_3 &: \min\{\text{dist}_{(i,j)}\} - \text{Dist}_{\text{min}} \le 0 \end{aligned} \tag{3}$$

where n_{tur} is the number of turbines within each farm; N_{max} and N_{min} are, respectively, the maximum and minimum numbers of turbines; $dist_{(i,j)}$ is the Euclidean distance from turbine i to turbine j and $Dist_{min}$ represents the minimum distance to include a safety margin to account for floater moorings and operations safety.

Following the random creation of the first generation, the evaluation of individuals is carried out using the criterion outlined in [41]. Dominant individuals, also known as Pareto optimal, are those that meet all constraints and for which there is no other individual capable of outperforming them in both objective functions. Between two of such individuals, to preserve diversity, the one belonging to a less dense area in the space defined by f_1 and f_2 is preferred [41]. Once selected, the parents are mated with each other through the Binary Crossover mechanism illustrated in [42]. Thus, for each individual created, a mutation occurs with a probability determined by the P_{m1} parameter. The probability that the ith element of the binary array that describes the individual undergoes mutation is given by the P_{m2} parameter. The offspring generated are compared with the parent generation, and the best individuals from both groups are selected to compose the next generation. The number of individuals in each generation remains constant from the first to the last. This whole process is repeated until the last generation is created.

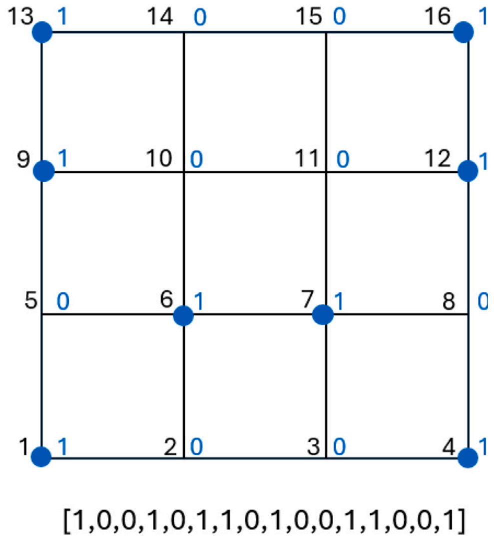

Fig. 1. Binary list representation of layout.

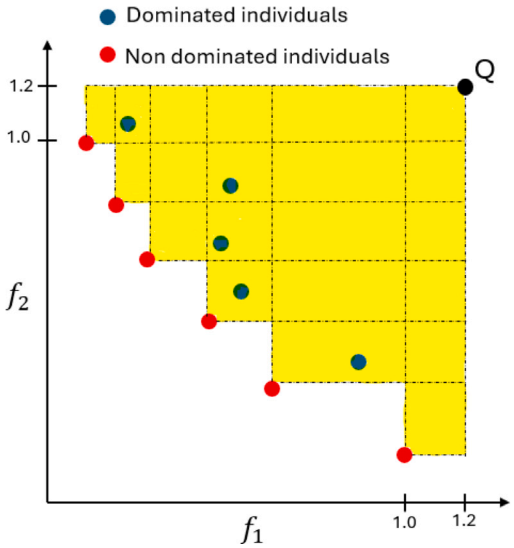

Fig. 2. Hypervolume, dominated and non-dominated individuals representation in a two-dimensional objective space.

The convergence of the algorithm is evaluated through the calculation of the hypervolume (HV), as defined in [43], for each generation. Fig. 2 shows, with reference to what has been explained, a two-dimensional objective space. Non-dominated individuals and dominated individuals are respectively reported in red and blue. In yellow is highlighted the HV area in the case where the reference point is set to $(1.2, 1.2)$. The dominated individuals do not contribute to the increase of HV, that is a global indicator of the quality of the solutions found.

2.2. Visual impact model

Visual impact is quantified using a model derived from [40]. In this work, multiple observation points are considered, and for each of them, the Visual Impact (VI) indicator, as defined below, is calculated. The algorithm starts determining the portion of the Field of View (FoV) occupied by the turbines, as represented in Fig. 3, specifically by projecting them onto the Surface of Projection (SoP), whose coordinates

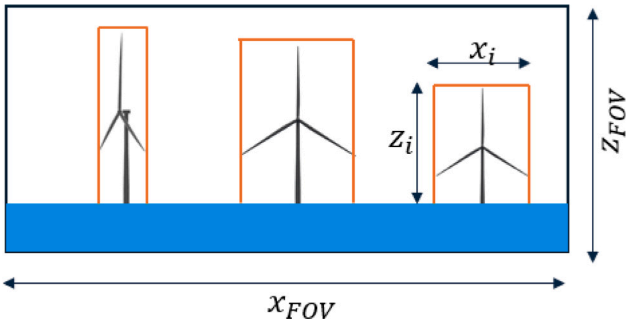

Fig. 3. Projections of the turbines within the FoV.

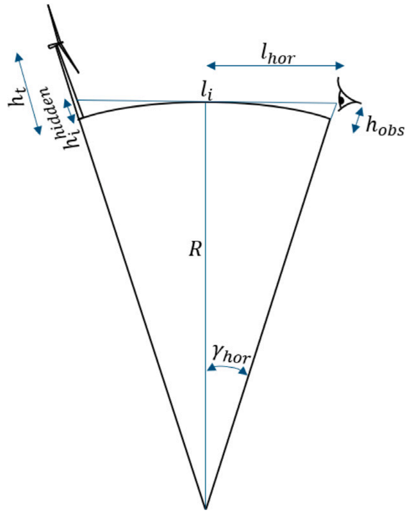

Fig. 4. Geometric representation of visibility analysis, according to [40].

are defined according to [40] as:

$$x_{\mathrm{FOV}} = \frac{120\pi}{180}\ [\mathrm{m}] \qquad z_{\mathrm{FOV}} = \frac{40\pi}{180}\ [\mathrm{m}] \tag{4}$$

The main distances and angle used in the next steps are represented in Fig. 4. The distance of the horizon from the observation point (l_{hor}) can be expressed, as a function of the observation point height (h_{obs}), by the following formula:

$$l_{\mathrm{hor}} = R\,\gamma_{\mathrm{hor}} = R\ \arccos\left(\frac{R}{R+h_{\mathrm{obs}}}\right) \tag{5}$$

where γ_{hor} is the angle between the horizon and the observation point, while R represents the Earth radius, estimated as $6.6371 \times 10^3\ km$. In case the turbine is located beyond l_{hor}, it is necessary to consider the effect of the Earth's curvature. As a result, a portion (h_i^{hidden}) of the height of the vertical projection of the turbine (h_t) will be obscured from the observers' view. Therefore, the length of the visible projection can be evaluated as:

$$z_i = \frac{h_t + r_t - h_i^{\mathrm{hidden}}}{l_i} \tag{6}$$

where r_t is the rotor radius and l_i represents the distance from the ith turbine to the observation point. h_i^{hidden} can be computed as:

$$h_i^{\mathrm{hidden}} = \frac{R}{\cos\left(\frac{l_i}{R} - \gamma_{\mathrm{hor}}\right)} - R \tag{7}$$

The reference model [40] is extended to include the dependency of the width of the horizontal projection of the rotor on the orientation of the rotors, as they point the axis in the direction of the upcoming wind. Therefore, the horizontal extent of the ith turbine is found as a function of the wind direction (θ) as:

$$x_i = \frac{D}{l_i}\cos(\varphi_i^{\mathrm{rot}}) \tag{8}$$

with D being the rotor diameter and $\varphi_i^{\mathrm{rot}} = \theta - \psi_i$, where

$$\psi_i = \arctan\left(\frac{X_i - x_{\mathrm{obs}}}{Y_i - y_{\mathrm{obs}}}\right) \tag{9}$$

being X_i and Y_i the geographical coordinates of the turbine and x_{obs} and y_{obs} the coordinates of the observation point. Finally, considering that the SoP is cylindrical, the coordinate of the ith turbine (X_i^{SoP}) on the SoP is obtained:

$$X_i^{\mathrm{SoP}} = \psi_i - \arctan\left(\frac{x_c - x_{\mathrm{obs}}}{y_c - y_{\mathrm{obs}}}\right) \tag{10}$$

where (x_c, y_c) represents the position of the centre of the wind farm. From the coordinate of the single turbine on the SoP (X_i^{SoP}) and the horizontal extension of the surrounding rectangle (x_i), the total area (A) can be computed. Specifically, A is the union of rectangles representing the approximated area occupied by each turbine on the SoP for the jth wind direction. Finally, visual impact is calculated for each of the 12 wind directions considered, and then multiplied by the frequency of occurrence of that direction, denoted as $f(\theta)$, through the following formula:

$$\mathrm{VI} = \frac{\sum_{j=1}^{12} A_j \cdot f(\vartheta_j)}{x_{\mathrm{FOV}}\,y_{\mathrm{FOV}}} \tag{11}$$

Fig. 3 illustrates how the FoV portion is occupied by the turbines and how their orientation affects the horizontal footprint.

When multiple observation points are considered, final VI is obtained by averaging the values calculated at each point. If all points are equally important as in this work, a simple arithmetic mean is used; otherwise, a weighted mean is applied to reflect their varying significance. A possible further extension of the model is to apply a weighting methodology based on the so-called "Spanish method" [44], which accounts for factors such as public exposure, landscape relevance, and social acceptance.

Fig. 5 provides a view of a sample wind farm consisting of 20 wind turbines, each with a capacity of 15 MW. In particular, Fig. 5(a) shows the locations of the turbines and the various observation points. Meanwhile, Fig. 5(b) provides a rendered visualization of the same wind farm along the horizon line from a point located 9 km from the centre of the farm.

2.3. *Annual Energy Production model*

FLORIS library [32] is used to compute the velocity field and the Annual Energy Production (AEP) of the wind farm corresponding to each individual. FLORIS is an open source tool developed by the National Renewable Energy Laboratory (NREL) and TU Delft to model turbine rotor-wake interactions within a wind farm using engineering wake models. In particular it is based on a discretization of the spatial domain through a grid of points located on the rotor plane. This approach accounts for heterogeneous inflow conditions due to the wind speed profile and the potential partial wake effects from upwind turbines by computing a spatially weighted average of the wind speeds across the grid points. This method allows for fast computation of the velocity fields and consequently of the farm's power production under each wind condition. This tool has been validated in terms of the prediction of power and velocity deficits due to WT wake, comparing its results with those obtained by large eddy simulations (LES) performed with SOWFA (Simulator fOr Wind Farm Applications) and with Supervisory Control and Data Acquisition (SCADA) data [31,45].

Several wake models are available in FLORIS. Among them, the Gauss Curl Hybrid model (GCH) is used in this work, setting up the

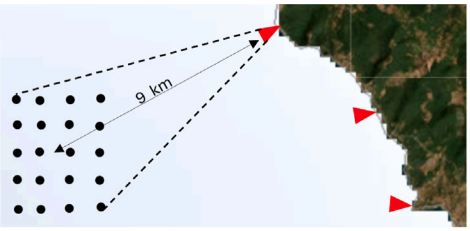

(a) Observation points and their relative positioning along the coastline.

(b) Rendered representation of the wind farm along the horizon line.

Fig. 5. Visualization of observation points and wind farm arrangement along the horizon line.

model parameters as reported in [46]. It combines the advantages of the Gaussian model of Bastankhah and Porté-Agel [29] and Niayifar and Porté-Agel [30] derived from the Gaussian approximation of the wake, and the Curl model described in [47] which adds information regarding the presence of vortices.

The streamwise velocity u_G is defined by the function:

$$\frac{u_G(x,y,z)}{U_\infty} = 1 - Ce^{-\frac{(y-\delta)^2}{2\sigma_y^2}} e^{-\frac{(z-z_h)^2}{2\sigma_z^2}} \tag{12}$$

where U_∞ is the freestream velocity, δ the wake deflection, σ_y and σ_z the wake width in the y and z directions respectively, z_h the hub height and C is the velocity deficit, defined as:

$$C = 1 - \sqrt{1 - \frac{C_T(\sigma_{y0}\sigma_{z0})}{\sigma_y \sigma_z}} \tag{13}$$

being C_T the trust coefficient which is function of U_∞ through the turbine thrust characteristic curve. The subscript “0” refers to the values at the beginning of the far wake, that corresponds to the point at which self-similarity is achieved [29]:

$$\frac{x_0}{D} = \frac{\cos y(1+\sqrt{1-C_T})}{\sqrt{2\left[4\alpha TI + 2\beta(1-\sqrt{1-C_T})\right]}} \tag{14}$$

here y is the yaw offset, assumed to be zero; α and β are fixed parameters set to 0.58 and 0.077 respectively, and TI is the turbulence intensity.

The wake widths can be estimated through:

$$\frac{\sigma_z}{D} = k_z \frac{x-x_0}{D} + \frac{\sigma_{z0}}{D} \quad \text{where} \quad \frac{\sigma_{z0}}{D} = \frac{1}{2}\sqrt{\frac{u_R}{U_\infty + u_0}} \tag{15}$$

$$\frac{\sigma_y}{D} = k_y \frac{x-x_0}{D} + \frac{\sigma_{y0}}{D} \quad \text{where} \quad \frac{\sigma_{y0}}{D} = \frac{\sigma_{z0}}{D}\cos y \tag{16}$$

where u_R is the flow velocity immediately after the rotor, u_0 the velocity at the start of the far wake region, and k_y and k_z are the wake expansion rates in the lateral and vertical directions respectively. Assuming identical expansion rates in both lateral and vertical directions, these latter two parameters are set to be the same and derived from TI:

$$k_{y,z} = k_a TI + k_b \tag{17}$$

With $k_a = 0.38$ and $k_b = 0.004$.

TI is calculated as a function of the ambient turbulence intensity and considering an extra component accounting for the influence of upstream turbines operations, as proposed in [30,48]. Wake deflection is considered as the combination of yaw misalignment, set as zero, and rotor-boundary layer interaction, obtained by [45] from an empirical relation. Wakes are finally combined with the sum-of-squares method [49]. In order to validate the model, in the Results section, findings obtained for the analysed case study with the aforementioned wake model are compared with those obtained using the simpler linear wake expansion model proposed by Jensen [28].

2.3.1. Wind turbine derating model

Another source of losses that affect the AEP of the wind farm is given by the performance derating associated to Leading Edge Erosion (LEE) on turbine blades. The erosion results from the high-speed collisions of the blade with rain droplets and hail stones that frequently occur during the power plant’s operational lifetime. This phenomenon leads to a reduction in lift and an increase in the drag forces on the blade which results in a reduction in the torque at the rotor hub and in a decrease in the produced power. It is estimated that LEE can cause an AEP loss ranging from 1% to 4% [50–52].

In order to include the LEE effect in the computation of AEP, in this work, a modification of the turbine power curve is applied at a constant rate. In particular, losses related to the last operational year of turbines are derived from simulation results recently published in literature, and, in particular, available from [53]. In the latter work, the dependence of power losses with the wind speed have been computed and reported for a 5 MW wind turbine with severely damaged blades. This result is here assumed as occurring at the end of the turbine life. As a first approximation, the average power loss fraction (percentage of power loss per wind speed) at the end of turbine life is assumed to be of the same value for a 5 MW and a 15 MW wind turbine. The value of the power loss fraction at intermediate years is then obtained by linear interpolation between the nominal power curve (at the first year of operation) and the severely damaged power curve (at end of life) at the year of interest.

2.4. Cost model

Included within capital expenditures are development and consent costs, which cover all the pre-construction surveys, including environmental, seabed and climate assessments, as well as project management

Table 1
Mooring components costs.

Parameter	Value	Unit	Reference
n_{lines}	3	–	[38]
MBL_{lines}	22 286	kN	[38]
MBL_{anchor}	9800	kN	[37]
f_{USD-e}	0.92	–	[55]

Table 2
Transmission components costs.

Parameter	Value	Unit	Reference
C_{ExCab}	2.336	M€/km	[34]
C_{SubOff}	39	M€	[34]
C_{IntArr}	303.5	k€/km	[34]

and consent services for the project. According to [34], their value is estimated to be 210 k€/MW. The major cost driver of CAPEX is related to the turbine and substructure. In this study, the average cost of a wind turbine and the semi-submersible platform are taken from [34] and set to 1.6 M€/MW and 8 M€ respectively. To secure the turbine and substructure to the seabed, a set of three catenary mooring lines per turbine is employed, anchored through Drag Embedment Anchors (DEA). The cost of this configuration can be computed according to [54] as:

$$C_m(x,y) = n_{tur} n_{lines}[(0.0591 \cdot MBL_{lines} - 87.69)H + 10.198 \cdot MBL_{anchor}] \cdot f_{USD-€} \tag{18}$$

where n_{lines} is the number of lines per turbine, H is the chain length, MBL_{lines} and MBL_{anchor} are the Minimum Breaking Loads of the chain and the anchor respectively and $f_{USD-€}$ the conversion factor from USD to €. Table 1 shows the values of these parameters.

The total cost of the electric infrastructure can be expressed, according to [34], as:

$$C_t(x,y) = d(x,y) n_{ExCab} C_{ExCab} + n_{SubOff} C_{SubOff} + l_{IntArr} C_{IntArr} \tag{19}$$

where $d(x,y)$ is the distance from the shore and n_{ExCab} and n_{SubOff} are the number of export cables and offshore substations respectively. The number of export cables (n_{ExCab}) is determined by assuming one cable every 300 MW of farm power. l_{IntArr} is the length of inter array cables, while the costs of export cables, offshore substation and inter array cables are denoted as C_{ExCab}, C_{SubOff} and C_{IntArr} and their values are provided in Table 2.

Installation costs are modelled as proposed by [34], incorporating adjustments suggested by [35]. In particular, the tower and floater are assumed to be preassembled onshore and transported on site by an Anchor Handling Tug Supply (AHTS) vessel, while the turbines are carried through a Platform Supply Vessel (PSV). The cost calculation is expressed as follows:

$$C_{InTur} = C_{vessel}\left[\frac{2d(x,y)}{V_{AHTS}} n_{TripsFl} + \frac{2d(x,y)}{V_{PSV}} n_{TripsTur} + T_{in} n_{tur}\right] \tag{20}$$

where C_{vessel} is the charter cost of a generic installation vessel, V_{AHTS} and V_{PSV} are the velocities of AHTS and PSV, T_{in} is installation time and $n_{TripsFl}$ and $n_{TripsTur}$ are the number of trips needed to transport floaters and turbines respectively. These last two values are computed knowing the number of floaters and turbines that the boats can transport ($n_{FlPerTrip}$ and $n_{TurPerTrip}$) as:

$$n_{TripsFl} = \frac{n_{fl}}{n_{FlPerTrip}} \tag{21}$$

$$n_{TripsTur} = \frac{n_{tur}}{n_{TurPerTrip}} \tag{22}$$

being n_{fl} the total number of floaters, same as n_{tur}. Table 3 lists the adopted quantities.

Table 3
Turbines installation components costs.

Parameter	Value	Unit	Reference
C_{vessel}	0.012	M€/h	[36]
V_{AHTS}	10	km/h	[35]
V_{PSV}	61.7	km/h	[35]
$n_{FlPerTrip}$	2	–	[35]
$n_{TurPerTrip}$	3	–	[35]
T_{in}	48	h	[34]

Table 4
Electric infrastructure installation components costs.

Parameter	Value	Unit	Reference
$C_{InSubOff}$	20	M€	[34]
$C_{InExCab}$	0.637	M€/km	[34]
$C_{InIntArr}$	0.115	M€/km	[36]

Installation costs of electric infrastructures is given by [34]:

$$C_{InElec} = C_{InSubOff} + C_{InExCab} \cdot l_{ExCab} \cdot n_{ExCab} + C_{InIntArr} \cdot l_{IntArr} \tag{23}$$

here $C_{InSubOff}$, $C_{InExCab}$ and $C_{InIntArr}$ are installation costs of the offshore substations, the export cables and the inter array cables respectively, while l_{IntArr} and l_{ExCab} are the length of inter array and export cables. The values are reported in Table 4.

The installation cost of the mooring system is set to 240 k€ per turbine as estimated in [34].

The decommissioning process consists of a reverse assembly process in which the components are dismantled, allowing for the sale of scrap metal and generating a minimal return. The value of the revenue is assumed as in the WindFloat project [39] as 230 k€/MW.

OPEX are influenced the most by the farm's location, which affects the distance between the wind farm and the maintenance facility, and by the site's metocean climate [54]. A value of 131 k€/MW is estimated as provided in [36]. The initial investment cost was validated against a planned offshore wind project along the Italian coast, showing a discrepancy of 2% [56].

3. Case study

In this work, the outlined method is employed for a virtual case study located in the Mediterranean Sea, 9 km off the coast of Civitavecchia, Lazio. For the selected site wind data are sourced from the Global Wind Atlas [33]. From the wind data, a wind rose associates a joint frequency of occurrence for each combination of wind speed and direction, referring to the height corresponding to the rotor hub. Moreover, the wind speed profile is obtained by using the power-law with a value of the wind shear exponent equal to 0.12. The latter value is consistent with the literature [57] for stable atmospheric conditions. The ambient turbulence intensity is taken from the FINO1 experiment [58], which relies on data collected from a mast positioned in the German Bight. This data comprises a series of turbulence values corresponding to different wind speeds. In particular, for wind speeds around 2 m/s, TI is 14%, decreasing to 5.9% as the wind speed reaches 10 m/s. Beyond this point, TI increases due to the intensification of wavelike motions, rising to 8.5% at wind speeds near 30 m/s.

The study area spans $20D \times 20D$, where D represents the rotor diameter of the turbine, equivalent to approximately 5 km × 5 km, and is characterized by the bathymetry shown in Fig. 6 together with the corresponding wind rose and the substation location. Moreover, the three numbered red crosses in figure indicate the locations of the observation points. The area is discretized with cells of 240 m side, leading to 441 possible locations for the turbines.

The characteristics of the site are listed in Table 5.

The values chosen for the constraints are 36 and 5 for the maximum and minimum number of turbines respectively and 3D for the minimum

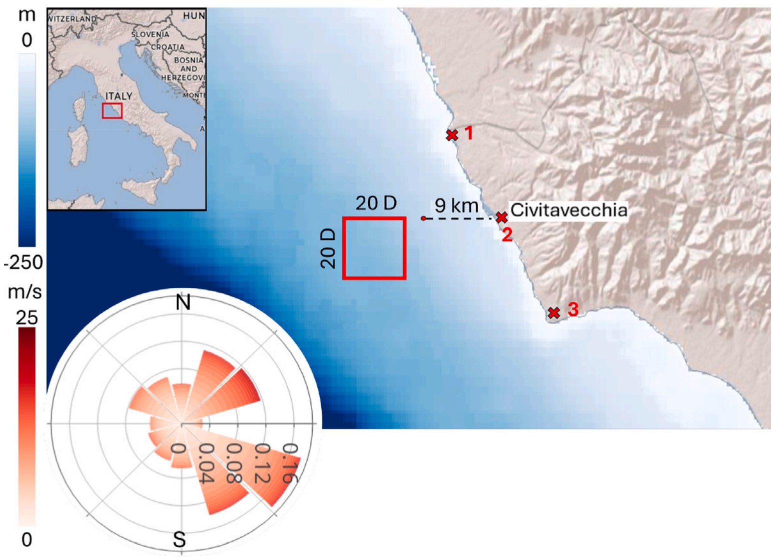

Fig. 6. Bathymetry map and wind rose for the case study.

Table 5
Site characteristics.

Parameter	Value
Most frequent wind direction	120°
Mean wind speed (at hub height)	7 m/s
Ambient turbulence intensity	[58]
Depth range	100–250 m
Shore distance	9 km
Port distance	10 km

distance between them. The first generation contains 1500 possible layout configurations and evolves for a total of 4000 generations. The mutation is defined by $P_{m1} = 0.5$ and $P_{m2} = 0.01$.

The selected turbine is the IEA 15 MW [59] reference turbine, operating in the wind speed range between 3 and 25 m/s (cut-in and cut-off wind speed). This turbine is characterized by a rotor diameter of 240 m, an hub height of 150 m and a rated wind speed of 10.59 m/s. Moreover, the turbine characteristic curves necessary for the calculation of the farm's power production under different inflow conditions, including the power coefficient and thrust coefficient, are known. For the wind farm, an expected lifespan of 25 years is assumed. Moreover, a discount rate of 5% is assumed for offshore wind projects.

Results obtained using the 15 MW turbine are finally compared with those obtained using the smaller NREL 5 MW wind turbine [60].

4. Results

Algorithm convergence is verified by evaluating the trend of the value assumed by the hypervolume indicator, which shows negligible variations at 4000 generations. Fig. 7(a) presents the convergence history in terms of the hypervolume indicator, while Fig. 7(b) shows a heatmap of the cumulative distribution of occupied positions by wind turbines within the optimization history. Fig. 7(b) clearly highlights how each available position has been occupied by turbines, thus each location has been part of an individual, and evaluated. In the picture, greater occurrence values indicate layout positions that survived the most over the generations. The definition of the clustered regions is in accordance with the steep growth of the HV curve in Fig. 7(a), indicating that the Pareto front consolidated around a solid population quite early.

Fig. 8 presents a graphical representation of the two objective functions, LCOE and VI, plotted against the number of turbines. Each point of both curves corresponds to the best-performing individual among all generations in terms of the lowest objective function value for a given number of turbines. Moreover, for turbine counts ranging from 5 to 19, the best-performing individuals among all generations also belong to the final generation and, so, to the final Pareto front. In contrast, individuals with a number of turbines greater than 19 (i.e. characterized by 20 WTs) do not appear in the final generation and have been discarded by the algorithm over successive generations. In the picture, non-optimal layouts characterized by a number of turbines greater than 19 are represented with crosses, while layouts belonging to the final generation are represented with circles. The blue line represents LCOE while the red line VI. Values of both functions are normalized by their maximum value. The LCOE curve reaches the minimum value corresponding to the case with 19 turbines. The initial steep slope of the curve is related to two factors: the almost direct proportionality between AEP and the number of turbines, due to the almost absence of wake losses, and the high impact of amortization of costs related to base infrastructure (substation, export cables). As the number of turbines increases, the latter factor gradually loses importance while the magnitude of wake losses increases. This leads to flattening of the curve until the point where the effect of the wakes completely offsets the advantage of amortizing infrastructure expenses. Therefore, this value represents the number of turbines that maximizes the economic potential of the area. Conversely, the visual impact exhibits a continuously rising trend together with turbines count. As shown in later Fig. 10(a), the layout with the lowest visual impact features a single row of turbines positioned along the side farthest from the coast. Given the length of this side and the minimum rotor-spacing constraint, five turbines fully occupy the available space along this edge. Consequently, as the number of turbines increases, additional turbines must be placed in a row closer to the coast, explaining the steep increase in visual impact when moving from five to six turbines. Conversely, further increasing turbine count results in a smaller increment in visual impact as additional rows are progressively filled. This process continues until the second row is filled and so on, with subsequent rows being added

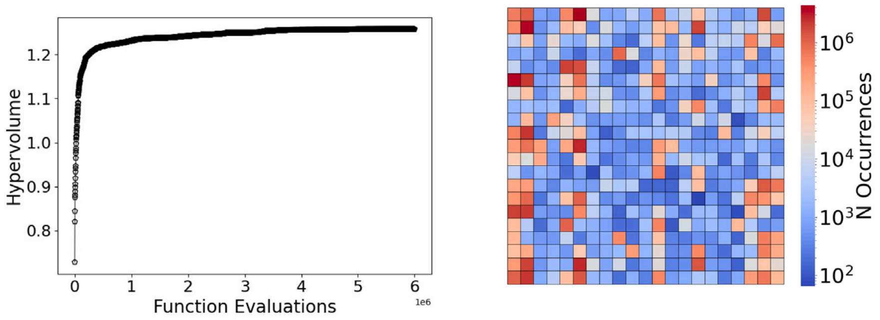

(a) Hypervolume indicator

(b) Occupied positions

Fig. 7. Convergence history.

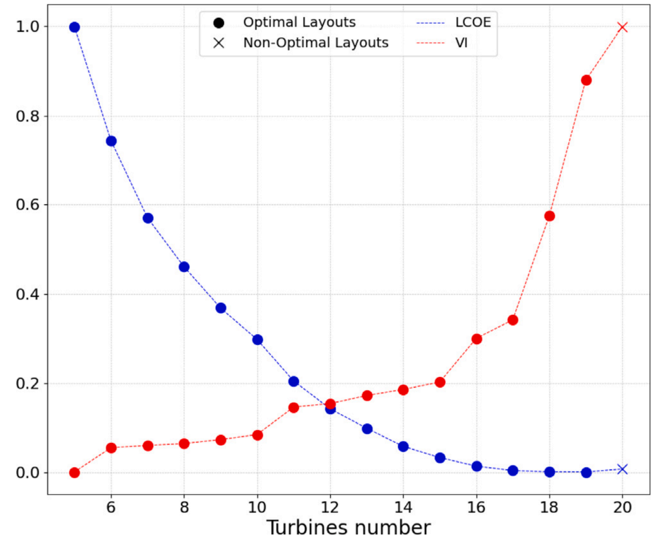

Fig. 8. Normalized LCOE (blue) and VI (red) for different number of turbines.

and completed. However, as the number of turbines increases beyond 17, the algorithm progressively prioritizes the LCOE minimization, which explains the irregular trend in the final part of the curve.

Moreover, considering results obtained in a previous work [18], where AEP and total costs were used as objective functions, it can be inferred that layouts characterized by the lowest LCOE values, given the same number of turbines, are the same ones that achieve the highest AEP values despite higher costs associated with turbine placement. Specifically, the benefit of reducing rotor interactions by increasing the spacing between turbines outweighs the additional costs related to the longer cable lengths or the greater local depth of the seabed.

Fig. 9 shows the Pareto front of optimal individuals belonging to the last generation. On the axes the two objective functions are represented. The colour of the plotted points indicates the number of turbines characterizing each layout. In the front there is no layout with more than 19 turbines despite the maximum limit being set at 36 rotors. Layouts with a greater number of turbines, in fact, present a higher VI, and, as previously explained, they turn out to be less cost-efficient. Furthermore, the Pareto front exhibits two areas with high sensitivity to the two objective functions: in the upper-left zone, a significant reduction in visual impact is achieved at the expense of a small increase in LCOE, while in the lower-right zone, the opposite is true. Fig. 9 also highlights three points of interest: the square denotes the point with the lowest VI (Case “a”); the triangle indicates the point with the lowest LCOE (Case “c”); and the cross represents the trade-off solutions representative (Case “b”). The latter is defined as the layout characterized by the minimum distance from the origin of the axis in the objective space. The decision to highlight this point is to display the most appealing solution in scenarios where the two objective functions are of equal interest.

Table 6
Comparison of the optimal individuals.

	Min VI	Trade-off	Min LCOE
n_{tur}	5	13	19
LCOE (€/MWh)	128.67	110.73	105.72
VI (normalized)	0	0.25	1
AEP (GWh)	232.17	603.64	895.05
Wake Losses (%)	4.57	4.56	3.18

Fig. 10 displays these three layouts and Table 6 lists their corresponding values of the objective functions. In Table 6 are also reported AEP and wake losses, defined as the percentage of energy lost due to interactions among the rotors.

In the layout with the minimum visual impact turbines are arranged along the side furthest from the coast. Case “b” exhibits a regular structure characterized by three rows of turbines. In this configuration, turbines visually shield each other, resulting in high wake losses. Case “c”, on the opposite, features an irregular distribution, driven by the need to maximize the energy production and minimize the rotor-wake interactions at the expenses of a significant VI.

Moreover, Fig. 11 provides insights into the effect of rotor orientation on visual impact. The three subplots, each corresponding to one of the three selected individuals, illustrate the variations in visual impact as a function of wind direction and, consequently, rotor orientation. The blue, orange, and green lines represent, referring to Fig. 6, the observation points “1”, “2” and “3”, respectively. The red line indicates the visual impact averaged across the three observation points, while the constant violet line represents the overall visual impact characteristic of the individual, computed as a frequency-weighted average. To maintain consistency with the results presented in Table 6, the values on the y axis are normalized using a min–max scaler, where the minimum and maximum values correspond to the global visual impact of the layout “a” and “c”, respectively. The curves clearly exhibit symmetry with respect to a 180° shift in wind direction, since for two wind directions separated by 180°, the rotor orientation remains the same. Moreover, it can be observed that observation point 1, which is located closer to the centre of the wind farm, consistently exhibits the highest maximum visual impact across all layouts. More interestingly, it also shows the largest variation in visual impact as wind direction changes. This is due to the greater influence of horizontal turbine visual footprint, particularly when turbines are positioned closer to

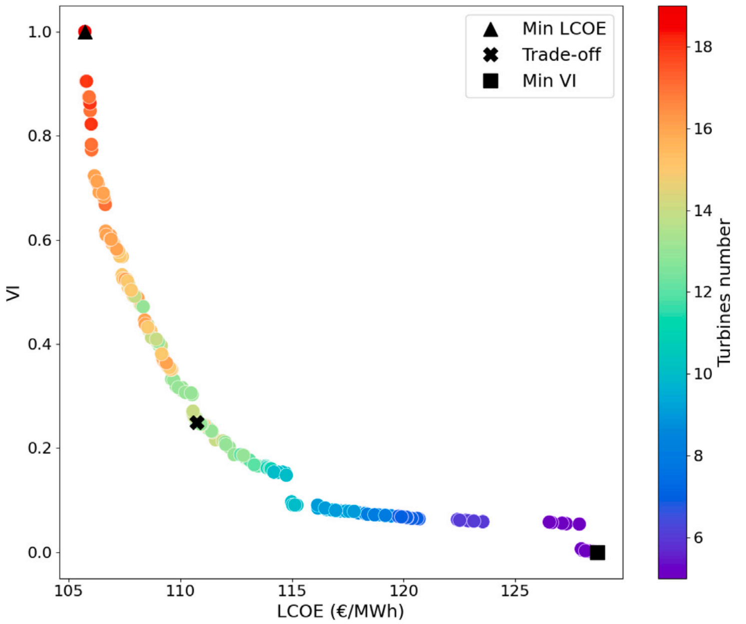

Fig. 9. Pareto front of dominant individuals.

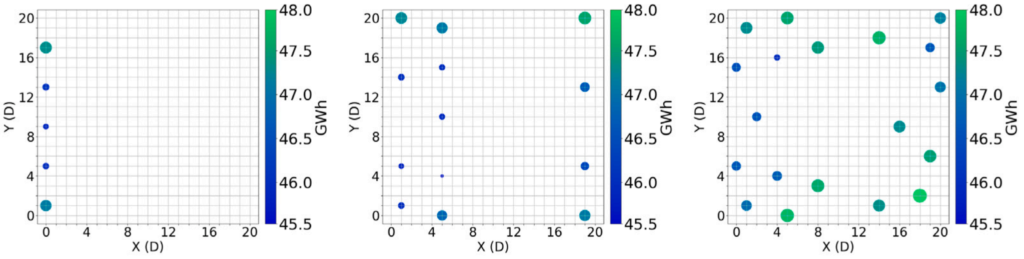

(a) (b) (c)

Fig. 10. Comparison of wind farm optimal layout configurations according to diverse optimum criteria: (a) minimum VI, (b) trade-off solution, and (c) minimum LCOE (colour scale and symbol diameter represent AEP).

the coastline. In addition, the curve trends remain quite similar across the different layouts, with maximum and minimum values occurring in the same wind directions. Finally, the average visual impact across the observation points (red line) exhibits significant oscillations in all three cases compared to the overall impact averaged across wind directions. In particular, focusing on the minimum LCOE layout, for a wind direction of 60°, the visual impact is 44% higher than the global average.

4.1. Effect of wake model choice

Results obtained with the previously discussed Gaussian wake model are compared with results obtained with the simpler and more established Jensen model [28]. For this model, an uncertainty analysis is conducted in [61] using bootstrap method, comparing results obtained with the analytical model with SCADA data from 10 offshore wind farms. The study reports an uncertainty range of 1.4% to 5% for 9 of the 10 wind farms, with one outlier exhibiting a value of 15%.

The value of the wake expansion coefficient is set to 0.05. The comparison is made with all parameters and constrains held constant. Fig. 12 illustrates the two fronts of optimal individuals: in red the individuals obtained with the GCH model, and in blue those obtained with the Jensen model. The VI values are normalized against the maximum obtained value. The two fronts almost overlap, particularly in the areas where the two objective functions exhibit high sensitivity. Moreover, in the area surrounding the knee point, the two curves diverge slightly: the Jensen model yields lower LCOE values due to its underestimation of wake losses compared to the GCH model. In both cases, the layouts that minimize LCOE consist of 19 turbines and result in very similar LCOE values: 105.39 €/MWh for the Jensen model and 105.72 €/MWh for the GCH model. Moreover, the similarity of the results obtained with the two models allows the uncertainty estimates derived for the Jensen model in [61] to be applied to the GCH model as well.

4.2. Effect of turbine choice

This section discusses and validates how the optimization can be affected if a smaller size turbine model is considered in the design of the wind farm. The NREL 5 MW reference turbine [60] is then selected to make a comparative study for the same test case. Throughout this study, all parameters set for optimization and constraints remain unchanged, while the substructure used is of the spar-buoy type, the cost of which is set at 3.74 M€ [35].

Fig. 13 displays the Pareto fronts obtained in both cases. In this graph, the VI values are normalized against the maximum value of the results obtained considering the 15 MW turbine. Layouts featuring 15 MW turbines are indicated with circles, while those using 5 MW turbines are marked with crosses. The colour of the markers indicates the number of turbines. The graph confirms the economic advantage

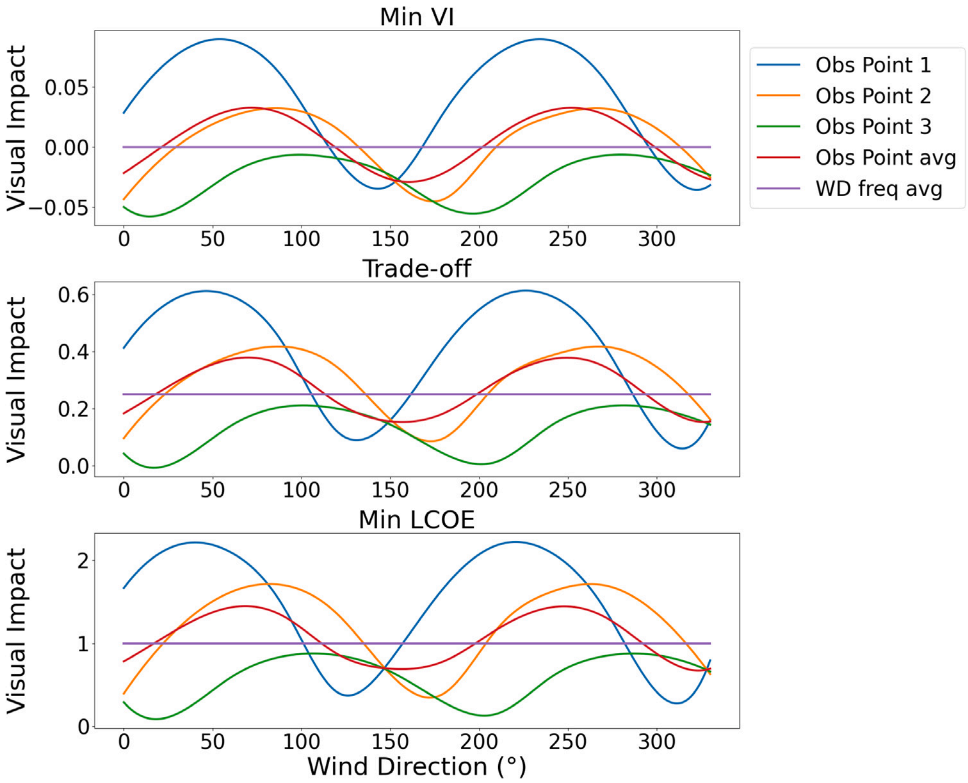

Fig. 11. Analysis of VI with the site wind rose distribution for the optimal wind farm layouts according to diverse optimum criteria. From top to bottom: (a) minimum VI, (b) trade-off solution, and (c) minimum LCOE.

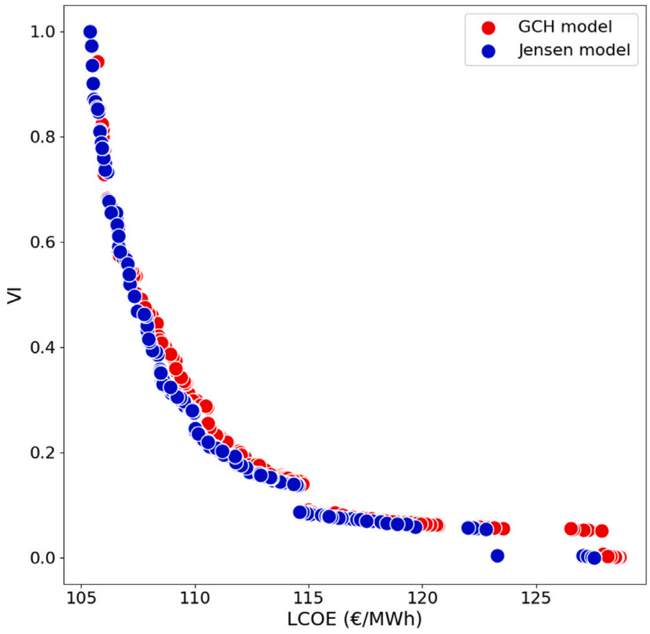

Fig. 12. Comparison of the Pareto fronts of the different wake models: Jensen (blue) and GCH (red).

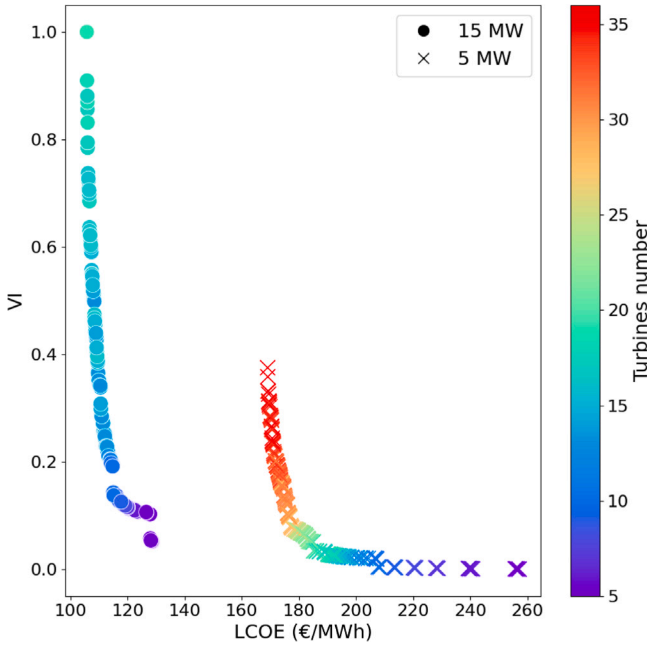

Fig. 13. Comparison of the Pareto fronts from individuals defined by different turbine models: IEA 15 MW (circle), NREL 5 MW (cross).

of installing larger turbines. This choice, in fact, allows for significant reduction in infrastructure and installation costs. On the other hand, the size of the turbines significantly affects their visual impact from the coast: configurations with 36 turbines of 5 MW have a visual impact that is comparable to configurations with less than half that number of 15 MW turbines. Furthermore, the layout with the lowest LCOE (169.05 €/MWh) in the case of choosing 5 MW turbines presents 36 turbines, corresponding to the maximum number allowed by the constraints of the problem. This results from the reduced wake interactions encountered with smaller rotors, coupled with the need to amortize infrastructure and installation costs.

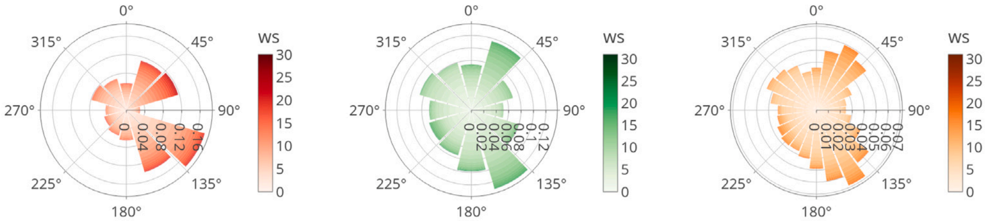

(a) GWA (b) ERA5 12 bins (c) ERA5 24 bins

Fig. 14. Wind roses from different data sources.

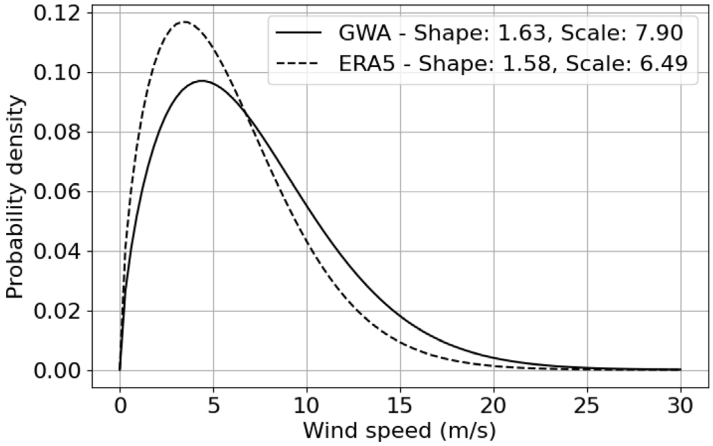

Fig. 15. Weibull probability density functions of wind speed obtained from GWA and ERA5 data.

4.3. Effect of using different wind data sources

This section discusses the impact of using different data sources on the optimization results. In addition to the statistical data derived from the Global Wind Atlas, historical wind data from the ERA5 database [62] are also used. For the latter, ten years of wind data are retrieved, including the east–west and north–south wind speed components at a height of 100 m. From these components, time series of wind direction and wind speed at hub height are derived using the power law with an exponent of 0.12. Based on these time series, two wind roses are generated. In the first case, the wind direction is divided into 12 bins of 30° each, while in the second, 24 bins of 15° are used. In both cases, wind speed bins are set to 1 m/s. Fig. 14 presents the three resulting wind roses: the red wind rose corresponds to data from GWA, the green wind rose represents the ERA5 dataset with 12 directional bins, and the orange wind rose corresponds to the ERA5 dataset with 24 directional bins.

Moreover, Fig. 15 shows the Weibull distributions obtained from the two sources. The solid line represents the distribution derived from the GWA, while the dashed line corresponds to the one obtained from ERA5. The latter distribution exhibits a higher peak at lower wind speeds, indicating a greater frequency of low winds compared to GWA. Conversely, the GWA distribution has a slightly broader tail, suggesting a higher probability of stronger wind events. In particular, as shown in the figure, the GWA distribution is characterized by a shape parameter of 1.63 and a scale parameter of 7.9, while the ERA5 distribution has a shape parameter of 1.58 and a scale parameter of 6.49. Furthermore, the mean wind speed obtained from GWA is 7.06 m/s, which is more than 1 m/s higher than the value derived from ERA5, equal to 5.87 m/s.

Fig. 16 presents the fronts obtained from the three wind roses. The red points represent the layouts derived from the GWA dataset, the green points correspond to the layouts obtained from the ERA5 dataset using 12 wind direction bins, and the orange points represent the layouts derived from the same dataset using 24 bins. The VI values are normalized against the maximum obtained value. The observations regarding wind speed distributions are confirmed by the results obtained for the LCOE objective function values, as shown in the plot. Specifically, the ERA5 historical data series, which exhibit a higher occurrence of low wind speeds compared to the GWA dataset, result in higher LCOE values. Moreover, using narrower wind direction bins allows the algorithm to identify solutions with lower objective function values, particularly in the region of the front that is highly sensitive to LCOE and around the knee point. In contrast, in the region characterized by high VI sensitivity, the smaller bin width leads to an underestimation of wake losses compared to the 24-bin case, especially for solutions with a high number of turbines. The solution with the lowest LCOE in the ERA5 case with 12 bins consists of 16 turbines, an AEP of 556.17 GWh, wake losses of 2.6%, and an LCOE of 147.71 €/MW. In the ERA5 case with 24 bins, the most economically advantageous layout consists of 15 turbines, an AEP of 509.66 GWh, wake losses of 4.8%, and an LCOE of 152.03 €/MW.

4.4. Scalability

In order to explore the scalability of the proposed method, a scalability test is performed for increasing occupied sea areas. The area of the case study is considered as the reference area (A), and three additional optimization problems are solved, where the area increases linearly from 0.5 A to 2 A. Each layout optimization problem presents a discretization grid with larger side length, but the grid resolution is kept the same. Thus, the number of available locations for the wind turbines is increasing with the area, while the impact of the minimum distance constraint is reducing for larger areas. Table 7 presents the details of the four problem setups.

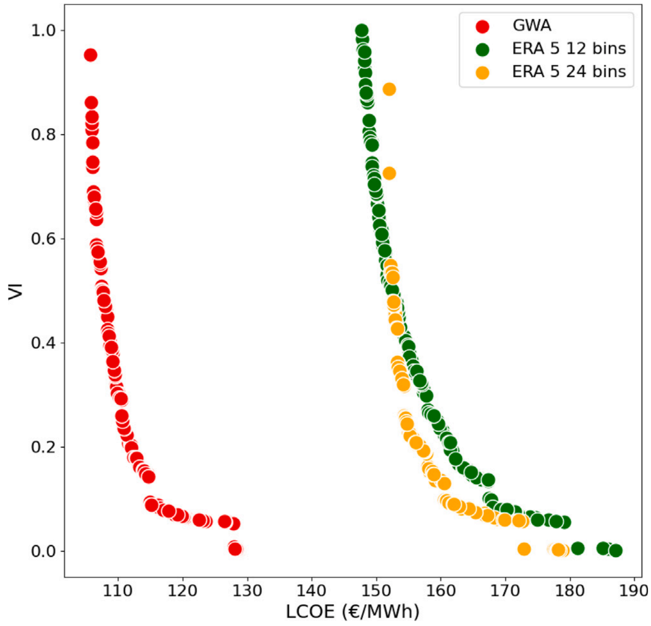

Fig. 16. Comparison of the Pareto fronts obtained from different data sources and using different wind directions bins: GWA (red), ERA5 with 12 direction bins (green) and ERA5 with 24 direction bins (orange).

Table 7
Comparison of the scalability tests.

	0.5 Area	1 Area	2 Area
Area	11.52	23.04	45.96
Available locations	225	441	900
n_{tur} (min–max)	2–13	5–19	10-21
$LCOE_{min}$ (€/MWh)	109.01	105.72	104.12
AEP_{max} (GWh)	613.34	895.05	1000.04
$Wake\ Losses_{min}$ (%)	3.03	3.18	2.19

Fig. 17 shows the comparison of the Pareto fronts of the three populations resulting from the scalability tests. The shape of the Pareto fronts is in general similar amongst the three different areas. Optimal population for the larger area is presenting reduced LCOE for equivalent VI, for wind farms with a slightly larger number of turbines with respect to the benchmark case. On the other hand, optimal population for the smaller area is presenting, for the same LCOE, a higher VI with a comparable number of turbines. The former is explained by the possibility for turbines to be placed in larger numbers due to the increased available area while still being in the furthest portion of the wind farm with respect to the observers. The latter is explained considering that the same number of turbines can only be placed in a smaller area by gradually filling regions closer to the observer, increasing VI.

The individuals for the three fronts can be compared by observing the cumulative distributions of turbine positions for the entire Pareto populations. Fig. 18 shows the three populations corresponding to the three areas of the scalability test, where each heatmap is representing on a $n \times n$ grid the discretized areas, while colour is representing the number of occurrences a turbine occupies that specific grid position within the whole Pareto population. It is possible to observe that the most frequent occupied positions are in general in the same regions for the three areas.

In Fig. 17 it is possible to highlight a cluster of individuals in the region close to the origin representing the trade-off populations, specifically in the LCOE range between 110 and 113 €/MWh and VI between 0.1 and 0.2, where the three populations present individuals with a similar number of turbines. Fig. 19 shows the cumulative layouts for the three different areas including individuals in the trade-off region comprised in the aforementioned objective function range. Specifically, the three heatmaps are counting respectively 27, 32 and 31 individuals in the described range. In contrast with the smaller areas, the larger area presents wind turbines concentrated in the furthest regions of the wind farm with respect to the observers. This is due the fact that for a comparable LCOE (and consequently number of turbines) with respect to the others, the larger wind farm is allowing for longer parallel rows of wind turbines that are minimizing VI being at a greater distance from the shore.

5. Conclusion

This work addresses the optimization of offshore wind farm layouts to support industrial-scale planning, providing a more size-agnostic approach than traditional designs. In fact, in the proposed method the number of turbines (thus the wind farm nominal power) is an independent variable of the optimization problem, and an output of the algorithm. This allows the wind farm to be better coupled with the site given the provided constraints and objectives. Additionally, unlike standard layouts driven primarily by economic considerations, this approach integrates both economic and social factors, specifically the visual impact from the coast. Given the growing importance of public acceptance in the deployment of offshore wind energy, incorporating social aspects into the design process is essential. To achieve this, the multi-objective optimization algorithm NSGA-II is applied using PyMoo, minimizing both LCOE and visual impact of a wind farm near the port of Civitavecchia (RM). Visual impact is quantified as the average portion of the field of view effectively occupied by the turbines calculated from three distinct observation points located along the coast, while the AEP estimation is made using the GCH engineering wake model implemented in FLORIS. The constraints are set as the minimum distance between turbines (equal to 3 diameters) and the admissible interval of turbines (between 5 and 36). Results show that the layout with the minimum VI consists of 5 turbines aligned along the side furthest from the coast, with LCOE of 128.67 €/MWh, and 4.57% wake losses. The layout closer to the origin of the axes can be considered as a representative of the trade-off region of the Pareto front is composed of 13 turbines positioned with a regular structure, with LCOE equal to 110.73 €/MWh, a normalized VI of 0.25 and 4.56% wake losses. Finally, the layout with minimum LCOE is characterized by 19 turbines irregularly positioned, with a LCOE of 105.72 €/MWh, the maximum VI and 3.18% wake losses, reflecting the prioritization of resource utilization over visual impact.

Additionally, four sensitivity analysis are performed to assess the impact of changing the wake model, the turbine size, the wind data source and the wind farm area. In the first case, the comparison of the Pareto fronts revealed a slight difference, with LCOE values being slightly lower when the Jensen wake model is selected instead of the Gaussian Curl Hybrid model. The second comparison indicates that the Pareto front shifts towards greater economic advantages when installing 15 MW turbines instead of 5 MW turbines, while the visual impact is significantly reduced with smaller turbines. Regarding the impact of different wind data sources, the analysis reveals the ability of the method to adapt to different wind speeds and directions, given that the wind derived from ERA5 exhibits a lower wind intensity compared to Global Wind Atlas, leading to higher LCOE values. Furthermore, the comparison between ERA5 wind discretized with 12 and 24 wind direction bins highlights that using narrower bins allows the algorithm to identify solutions characterized by lower values of the objective functions, particularly in the LCOE-sensitive region of the Pareto front. However, in the high visual impact sensitivity region, which includes layouts with a high number of turbines, the 12-bin case underestimates wake losses compared to the 24-bin case. Finally, the analysis performed to evaluate the adaptation capacity of the method to variation in the size of the occupied area of the wind farm, led to

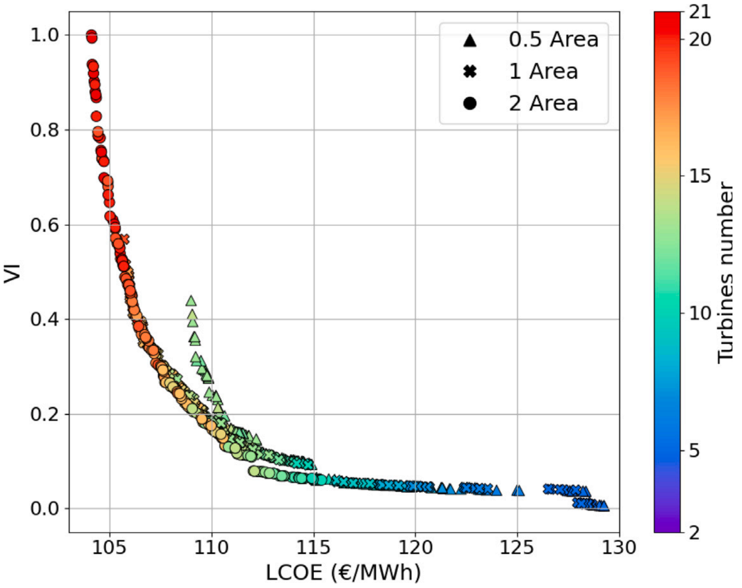

Fig. 17. Comparison of the different Pareto fronts for the scalability tests.

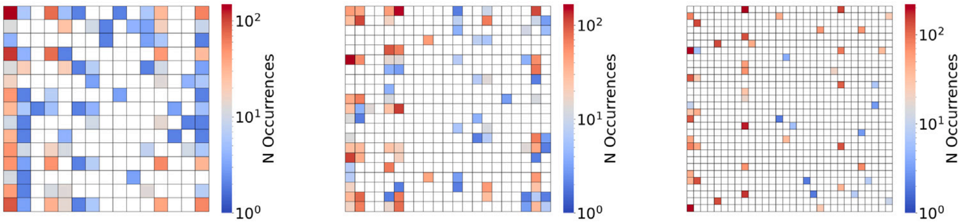

(a) 0.5 Area (b) 1 Area (c) 2 Area

Fig. 18. Cumulative distribution of the layouts within each Pareto population for the three different areas: (a) 0.5 Area, (b) 1 Area and (c) 2 Area.

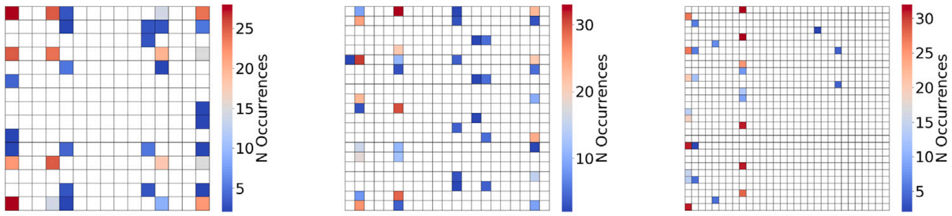

(a) 0.5 Area (b) 1 Area (c) 2 Area

Fig. 19. Cumulative distribution of the layouts in the trade-off region for the three different areas.

further confirmation of the behaviour of the optimizer in the trade-off region of the function space.

CRediT authorship contribution statement

V.F. Barnabei: Writing – review & editing, Methodology, Funding acquisition, Conceptualization, Supervision, Software, Investigation, Formal analysis. **M. Conti:** Writing – original draft, Formal analysis, Software, Writing – review & editing, Visualization, Investigation, Data curation. **T.C.M. Ancora:** Investigation, Data curation, Software, Writing – review & editing, Visualization, Methodology, Writing – original draft, Formal analysis. **G. Delibra:** Methodology, Supervision, Conceptualization. **A. Castorrini:** Investigation, Writing – review & editing, Supervision, Writing – original draft, Methodology, Conceptualization. **F. Rispoli:** Funding acquisition, Writing – review & editing, Project administration, Supervision. **A. Corsini:** Writing – review & editing, Funding acquisition, Project administration, Supervision.

Declaration of competing interest

The authors declare that they have no known competing financial interests or personal relationships that could have appeared to influence the work reported in this paper.

Acknowledgements

This research is supported by the Italian Ministry of University and Research as part of the European Union program NextGenerationEU, PNRR - M4C2 - PE0000021 ”NEST – Network 4 Energy Sustainable Transition” in Spoke 2 ”Energy Harvesting and Off-shore renewables”.

Data availability

Data will be made available on request.

References

[1] European Commission, Directorate-General for Climate Action. Going climate-neutral by 2050 – a strategic long-term vision for a prosperous, modern, competitive and climate-neutral eu economy. Publications Office; 2019, URL https://data.europa.eu/doi/10.2834/02074.

[2] European Commission. Repowereu plan. Communication from the commission to the European parliament, the council, the European economic and social committee and the committee of the regions. 2022, COM(2022) 230 final.

[3] European Commission. Delivering on the EU offshore renewable ambitions. 2023, COM(2023) 668 final, Available from: European Commission, 2023, Communication from the Commission to the European Parliament, the Council, the European Economic and Social Committee and the Committee of the Regions.

[4] McCoy A, Musial W, Hammond R, Mulas Hernando D, Duffy P, Beiter P, et al. Offshore wind market report, Tech. rep., 2024th ed.. National Renewable Energy Laboratory (NREL), Golden, CO (United States); 2024.

[5] Bush D, Hoagland P. Public opinion and the environmental, economic and aesthetic impacts of offshore wind. Ocean & Coastal Management 2016;120:70–9.

[6] International Renewable Energy Agency (IRENA), Clean Energy Ministerial (CEM). Renewable energy auctions: A guide to design. 2015, [Accessed 01 March 2025].

[7] Westerberg V, Jacobsen JB, Lifran R. The case for offshore wind farms, artificial reefs and sustainable tourism in the french mediterranean. Tour Manag 2013;34:172–83.

[8] Hou P, Zhu J, Ma K, Yang G, Hu W, Chen Z. A review of offshore wind farm layout optimization and electrical system design methods. J Mod Power Syst Clean Energy 2019;7(5):975–86.

[9] Tesauro A, Réthoré P-E, Larsen GC. State of the art of wind farm optimization. In: EWEC 2012-European wind energy conference & exhibition. European Wind Energy Association (EWEA); 2012, p. 1–11.

[10] do Couto TG, Farias B, Diniz A, de Morais MVG. Optimization of wind farm layout using genetic algorithm. In: 10th world congress on structural and multidisciplinary optimization. 2013, p. 1–10.

[11] Pouraltafi-Kheljan S, Azimi A, Mohammadi-ivatloo B, Rasouli M. Optimal design of wind farm layout using a biogeographical based optimization algorithm. J Clean Prod 2018;201:1111–24.

[12] Yang Q, Li H, Li T, Zhou X. Wind farm layout optimization for levelized cost of energy minimization with combined analytical wake model and hybrid optimization strategy. Energy Convers Manage 2021;248:114778.

[13] Chen Y, Li H, He B, Wang P, Jin K. Multi-objective genetic algorithm based innovative wind farm layout optimization method. Energy Convers Manage 2015;105:1318–27.

[14] Guirguis D, Romero DA, Amon CH. Gradient-based multidisciplinary design of wind farms with continuous-variable formulations. Appl Energy 2017;197:279–91.

[15] Li W, Özcan E, John R. Multi-objective evolutionary algorithms and hyper-heuristics for wind farm layout optimisation. Renew Energy 2017;105:473–82.

[16] Biswas PP, Suganthan PN, Amaratunga GA. Decomposition based multi-objective evolutionary algorithm for windfarm layout optimization. Renew Energy 2018;115:326–37.

[17] Moreno SR, Pierezan J, dos Santos Coelho L, Mariani VC. Multi-objective lightning search algorithm applied to wind farm layout optimization. Energy 2021;216:119214.

[18] Barnabei VF, Ancora TCM, Conti M, Castorrini A, Delibra G, Rispoli F, et al. A multi objective optimization framework for offshore wind farm design in deep water seas. J Fluids Eng 2025;147(3):031105.

[19] Dinçer AE, Demir A, Yılmaz K. Multi-objective turbine allocation on a wind farm site. Appl Energy 2024;355:122346.

[20] Kim T, Song J, You D. Optimization of a wind farm layout to mitigate the wind power intermittency. Appl Energy 2024;367:123383.

[21] Zhang X, Wang Q, Ye S, Luo K, Fan J. Efficient layout optimization of offshore wind farm based on load surrogate model and genetic algorithm. Energy 2024;309:133106.

[22] Fischetti M, Monaci M. Proximity search heuristics for wind farm optimal layout. J Heuristics 2016;22:459–74.

[23] Gualtieri G. A novel method for wind farm layout optimization based on wind turbine selection. Energy Convers Manage 2019;193:106–23.

[24] Pollini N. Topology optimization of wind farm layouts. Renew Energy 2022;195:1015–27.

[25] Song J, Kim T, You D. Particle swarm optimization of a wind farm layout with active control of turbine yaws. Renew Energy 2023;206:738–47.

[26] Deb K, Pratap A, Agarwal S, Meyarivan T. A fast and elitist multiobjective genetic algorithm: NSGA-II. IEEE Trans Evol Comput 2002;6(2):182–97.

[27] Blank J, Deb K. Pymoo: Multi-objective optimization in python. Ieee Access 2020;8:89497–509.

[28] Jensen N. A note on wind generator interaction (risø-m-2411). Risø Natl Lab Rosk Den 1983.

[29] Bastankhah M, Porté-Agel F. Experimental and theoretical study of wind turbine wakes in yawed conditions. J Fluid Mech 2016;806:506–41.

[30] Niayifar A, Porté-Agel F. A new analytical model for wind farm power prediction. 625, IOP Publishing; 2015, 012039,

[31] Bay CJ, Fleming P, Doekemeijer B, King J, Churchfield M, Mudafort R. Addressing deep array effects and impacts to wake steering with the cumulative-curl wake model. Wind Energy Sci Discuss 2022;2022:1–28.

[32] National Renewable Energy Laboratory (NREL). FLORIS. 2023, Version 3.5.

[33] Davis NN, Badger J, Hahmann AN, Hansen BO, Mortensen NG, Kelly M, et al. The global wind atlas: A high-resolution dataset of climatologies and associated web-based application. Bull Am Meteorol Soc 2023;104(8):E1507–25.

[34] Martinez A, Iglesias G. Mapping of the levelised cost of energy for floating offshore wind in the European Atlantic. Renew Sustain Energy Rev 2022;154:111889.

[35] Myhr A, Bjerkseter C, Ågotnes A, Nygaard TA. Levelised cost of energy for offshore floating wind turbines in a life cycle perspective. Renew Energy 2014;66:714–28.

[36] Cavazzi S, Dutton A. An offshore wind energy geographic information system (OWE-gis) for assessment of the UK's offshore wind energy potential. Renew Energy 2016;87:212–28.

[37] Giglio E, Petracca E, Paduano B, Moscoloni C, Giorgi G, Sirigu SA. Estimating the cost of wave energy converters at an early design stage: A bottom-up approach. Sustainability 2023;15(8):6756.

[38] Allen C, Viscelli A, Dagher H, Goupee A, Gaertner E, Abbas N, et al. Definition of the UMaine VolturnUS-S reference platform developed for the IEA wind 15-megawatt offshore reference wind turbine (No. NREL/TP-5000–76773). National Renewable Energy Laboratory (NREL) Golden, CO (United States), Univ. of Maine Orono; 2020.

[39] Bjerkseter C, Ågotnes A. Levelised costs of energy for offshore floating wind turbine concepts. Norwegian University of Life Sciences, Ås; 2013.

[40] Gonzalez-Rodriguez AG, Serrano-Gonzalez J, Burgos-Payan M, Riquelme-Santos J. Multi-objective optimization of a uniformly distributed offshore wind farm considering both economic factors and visual impact. Sustain Energy Technol Assess 2022;52:102148.

[41] Kukkonen S, Lampinen J. GDE3: The third evolution step of generalized differential evolution. In: 2005 IEEE congress on evolutionary computation, vol. 1, IEEE; 2005, p. 443–50.

[42] Deb K, Sindhya K, Okabe T. Self-adaptive simulated binary crossover for real-parameter optimization. In: Proceedings of the 9th annual conference on genetic and evolutionary computation. 2007, p. 1187–94.

[43] Fonseca CM, Paquete L, López-Ibánez M. An improved dimension-sweep algorithm for the hypervolume indicator. In: 2006 IEEE international conference on evolutionary computation. IEEE; 2006, p. 1157–63.

[44] Manchado C, Gomez-Jauregui V, Otero C. A review on the spanish method of visual impact assessment of wind farms: SPM2. Renew Sustain Energy Rev 2015;49:756–67.

[45] Gebraad PM, Teeuwisse FW, Van Wingerden J, Fleming PA, Ruben SD, Marden JR, et al. Wind plant power optimization through yaw control using a parametric model for wake effects—a CFD simulation study. Wind Energy 2016;19(1):95–114.

[46] Annoni J, Fleming P, Scholbrock A, Roadman J, Dana S, Adcock C, et al. Analysis of control-oriented wake modeling tools using lidar field results. Wind Energy Sci 2018;3(2):819–31.

[47] Martínez-Tossas LA, Annoni J, Fleming PA, Churchfield MJ. The aerodynamics of the curled wake: a simplified model in view of flow control. Wind Energy Sci 2019;4(1):127–38.

[48] Crespo A, Herna J, et al. Turbulence characteristics in wind-turbine wakes. J Wind Eng Ind Aerodyn 1996;61(1):71–85.

[49] Katic I, Højstrup J, Jensen NO. A simple model for cluster efficiency. In: European wind energy association conference and exhibition. A. Raguzzi; 1987, p. 407–10.

[50] Cappugi L, Castorrini A, Bonfiglioli A, Minisci E, Campobasso MS. Machine learning-enabled prediction of wind turbine energy yield losses due to general blade leading edge erosion. Energy Convers Manage 2021;245:114567.

[51] Castorrini A, Ortolani A, Campobasso MS. Assessing the progression of wind turbine energy yield losses due to blade erosion by resolving damage geometries from lab tests and field observations. Renew Energy 2023;218:119256.

[52] Castorrini A, Barnabei VF, Domenech L, Šakalyté A, Sánchez F, Campobasso MS. Impact of meteorological data factors and material characterization method on the predictions of leading edge erosion of wind turbine blades. Renew Energy 2024;227:120549.

[53] Campobasso MS, Castorrini A, Ortolani A, Minisci E. Probabilistic analysis of wind turbine performance degradation due to blade erosion accounting for uncertainty of damage geometry. Renew Sustain Energy Rev 2023;178:113254.

[54] Beiter P, Musial W, Smith A, Kilcher L, Damiani R, Maness M, et al. A spatial-economic cost-reduction pathway analysis for US offshore wind energy development from 2015–2030. Tech. rep., National Renewable Energy Lab.(NREL), Golden, CO (United States); 2016.

[55] Bank EC. Euro foreign exchange reference rates USd. 2024, [Accessed 13 November 2024].

[56] Ministero dell'ambiente e della sicurezza energetica. Valutazioni e autorizzazioni ambientali: VAS - VIA - AIA. 2025, URL https://va.mite.gov.it/it-IT. [Accessed 06 February 2025].

[57] Albornoz CP, Soberanis ME, Rivera VR, Rivero M. Review of atmospheric stability estimations for wind power applications. Renew Sustain Energy Rev 2022;163:112505.

[58] Emeis S. Current issues in wind energy meteorology. Meteorol Appl 2014;21(4):803–19.

[59] Gaertner E, Rinker J, Sethuraman L, Zahle F, Anderson B, Barter GE, et al. IEA wind TCP task 37: definition of the IEA 15-megawatt offshore reference wind turbine. Tech. rep, National Renewable Energy Lab.(NREL), Golden, CO (United States); 2020.

[60] Jonkman J. Definition of a 5-MW reference wind turbine for offshore system development. Natl Renew Energy Lab 2009.

[61] Nygaard NG. Systematic quantification of wake model uncertainty. In: EWEA offshore conference. 2015, p. 10–2.

[62] Hersbach H, Bell B, Berrisford P, Biavati G, Horányi A, Muñoz Sabater J, et al. ERA5 hourly data on single levels from 1940 to present. Copernicus Climate Change Service (C3S) Climate Data Store (CDS); 2023, http://dx.doi.org/10.24381/cds.adbb2d47, [Accessed on 10 February 2025].